

Towards human Super EEG

Lucy L. W. Owen¹, Andrew C. Heusser^{1,2}, and Jeremy R. Manning^{1*}

¹Department of Psychological and Brain Sciences, Dartmouth College,
Hanover, NH 03755, USA

²Akili Interactive,
Boston, MA 02110, USA

Abstract

A growing body of literature over the past several decades reports that the dynamic correlational structure of functional neuroimaging data may be used to predict which moment of movie or story an individual is experiencing, identify which person's brain a recording came from, and identify the task a person is performing. However, our structural (anatomical) connectome is roughly static for the duration of typical neuroimaging experiments. How might these notions of dynamic functional connectomes versus static structural connectomes be reconciled? We use two human electrocorticographic (ECoG) datasets to ask: to what extent can we use a static connectome model (trained using within versus across subject data, and within versus across task data) to explain dynamic full-brain activity patterns? Given a fixed connectome model, and given recordings from a subset of brain locations, we test how reliably can one infer activity patterns throughout the rest of the brain. Our model-based approach, termed *SuperEEG*¹, is in itself useful for inferring full-brain activity patterns (at millimeter-scale spatial resolutions and millisecond-scale temporal resolutions) from ECoG recordings from a limited set of brain locations. For both datasets, we found that full-brain activity patterns can be best explained using connectomes from *other* people who performed a shared task.

Keywords: Electrocorticography (ECoG), intracranial electroencephalography (iEEG), local field potential (LFP), epilepsy, maximum likelihood estimation, Gaussian process regression

Are our brain's networks static or dynamic? And to what extent are the network properties of our brains stable across people and tasks? One body of work suggests that our brain's *functional*

¹The term "Super EEG" was coined by Robert J. Sawyer in his popular science fiction novel *The Terminal Experiment* [1]

networks are dynamic [e.g., 2], person-specific [e.g., 3], and task-specific [e.g., 4]. In contrast, although the gross anatomical structure of our brains changes meaningfully over the course of years as our brains develop, on the timescales of typical neuroimaging experiments (i.e., hours to days) our anatomical networks are largely stable [e.g., 5]. Further, many aspects of brain anatomy, including white matter structure, is largely preserved across people [e.g., 6–8]. There are several possible means of reconciling this apparent contradiction between dynamic person- and task-specific functional networks versus stable anatomical networks. For example, relatively small magnitude anatomical differences across people may be reflected in reliable functional connectivity differences. Along these lines, one recent study found that diffusion tensor imaging (DTI) structural data is similar across people, but may be used to predict person-specific resting state functional connectivity data [9]. Another (potentially complementary) possibility is that our functional networks are constrained by anatomy, but nevertheless exhibit rapid task-dependent changes [e.g., 10].

Here we take a model-based approach to studying whether high spatiotemporal resolution activity patterns throughout the human brain may be explained by a static connectome model that is shared across people and tasks. Specifically, we trained a model to take in recordings from a subset of brain locations, and then predict activity patterns during the same interval, but at *other* locations that were held out from the model. Our model, based on Gaussian process regression, relies on three assumptions (each of which we test). First, we assume that functional correlations are stable over time and across tasks. Second, we assume that some of the correlational structure of people’s brain activity is similar across individuals. Third, we resolve ambiguities in the data by assuming that neural activity from nearby sources will tend to be similar, all else being equal. After fitting the model to an ECoG dataset, one can then ask (for a held-out individual’s brain): given what we know about the correlational structure of *other* people’s brains, and given the recordings we made from electrodes implanted in this person’s

51 brain, how would those recordings most likely have looked at *other* locations throughout this
52 person’s brain? We named our general approach *SuperEEG* because the trained model provides
53 a means of inferring full-brain activity patterns at high spatiotemporal resolutions, using ECoG
54 recordings taken from a limited set of brain locations.

55 We tested the SuperEEG approach using two large ECoG datasets. Dataset 1 comprises
56 multi-hour recordings from 6876 electrodes taken across several recording sessions as 88 neu-
57 rosurgical patients studied random word lists periodically throughout their day [11–15]. Dataset
58 2 comprises recordings from XXX electrodes taken as XXX patients performed a series of two
59 memory tasks [16–24]. In both datasets, we compared the predictions made using models
60 trained across people to predictions made using within-person data. We found that models that
61 incorporate data from other patients yield far more reliable predictions about an individual pa-
62 tient’s brain activity patterns than models trained solely on that individual’s data. This indicates
63 that at least some functional correlations are common across people. We also used Dataset 2
64 to compare predictions made using data from within task, across task, or combining within and
65 across task data. We found that all three approaches yielded reliable predictions, but the within
66 task predictions were the most accurate. This indicates that some aspects of our functional
67 connectomes are common across tasks, whereas other aspects are task-specific. Finally, all of
68 the models we trained (within and across patients and tasks) assumed a static connectome and
69 yielded above-chance accuracy. This indicates that despite moment-by-moment fluctuations in
70 the functional connectome, at least some aspects of our connectome appear to be stable over the
71 course of several hours.

72 Approach

73 The SuperEEG approach to inferring high temporal resolution full-brain activity patterns is
74 outlined and summarized in Figure 1. We describe (in this section) and evaluate (in *Results*) our

approach using a two large previously collected dataset comprising multi-session intracranial recordings. The first dataset was taken from 6876 electrodes implanted in the brains of 88 epilepsy patients [11–15]. We first applied a fourth order Butterworth notch filter to remove 60 Hz ($\pm .5$ Hz) line noise. We then excluded any electrodes that showed putative epileptiform activity. Specifically, we excluded from further analysis any electrode that exhibited an average kurtosis of 10 or greater across all of that patient’s recording sessions. We also excluded any patients with fewer than 2 electrodes that passed this criteria, as the Super EEG algorithm requires measuring correlations between 2 or more electrodes from each patient. Altogether this yielded clean recordings from 4168 electrodes implanted throughout the brains of 67 patients (Fig. 1A). For the purposes of comparing task-specific contributions to reconstruction accuracy, we limited our analyses in the second dataset to patients that participated in two free recall experiments. Applying the same kurtosis thresholding yielded clean recordings from 24 patients and 2975 electrodes for the second dataset. Each individual patient contributes electrodes from a limited set of brain locations, which we localized in a common space (MNI152); an example patient’s 54 electrodes that passed the predefined kurtosis test are highlighted in black and red.

The recording from a given electrode is maximally informative about the activity of the neural tissue immediately surrounding its recording surface. However, brain regions that are distant from the recording surface of the electrode also contribute to the recording, albeit (often) to a much lesser extent. One mechanism underlying these contributions is volume conduction. The precise rate of falloff due to volume conduction (i.e. how much a small volume of brain tissue at location x contributes to the recording from an electrode at location η) depends on the size of the recording surface, the electrode’s impedance, and the conductance profile of the volume of brain between x and η . As an approximation of this intuition, we place a Gaussian radial basis function (RBF) at the location η of each electrode’s recording surface (Fig. 1B). We use the values of the RBF at any brain location x as a rough estimate of how much structures

100 around x contributed to the recording from location η :

$$\text{rbf}(x|\eta, \lambda) = \exp \left\{ -\frac{\|x - \eta\|^2}{\lambda} \right\}, \quad (1)$$

101 where the width variable λ is a parameter of the algorithm (which may in principle be set accord-
102 ing to location-specific tissue conductance profiles) that governs the level of spatial smoothing.
103 In choosing λ for the analyses presented here, we sought to maximize spatial resolution (which
104 implies a small value of λ) while also maximizing the algorithm's ability to generalize to any
105 location throughout the brain, including those without dense electrode coverage (which implies
106 a large value of λ). Using our prior work as a guide [25], we set $\lambda = 20$, although this could in
107 theory be optimized, e.g. using cross validation.

108 A second mechanism whereby a given region x can contribute to the recording at η is
109 through anatomical connections between structures near x and η . We use spatial correlations
110 in the data to estimate these anatomical connections. Let \bar{R} be the set of locations at which
111 we wish to estimate local field potentials, and let R_s be set of locations at which we observe
112 local field potentials from patient s (excluding the electrodes that did not pass the kurtosis test
113 described above). In the analyses below we define $\bar{R} = \cup_{s=1}^S R_s$. We can calculate the expected
114 inter-electrode correlation matrix for patient s , where $C_{s,k}(i, j)$ is the correlation between the
115 time series of voltages for electrodes i and j from subject s during session k , using:

$$\bar{C}_s = r\left(\frac{1}{n}\left(\sum_{k=1}^n z(C_{s,k})\right)\right), \text{ where} \quad (2)$$

$$z(r) = \frac{\log(1+r) - \log(1-r)}{2} \text{ is the Fisher } z\text{-transformation and} \quad (3)$$

$$z^{-1}(z) = r(z) = \frac{\exp(2z) - 1}{\exp(2z) + 1} \text{ is its inverse.} \quad (4)$$

116 Next, we use Equation 1 to construct a number of to-be-estimated locations by number of pa-

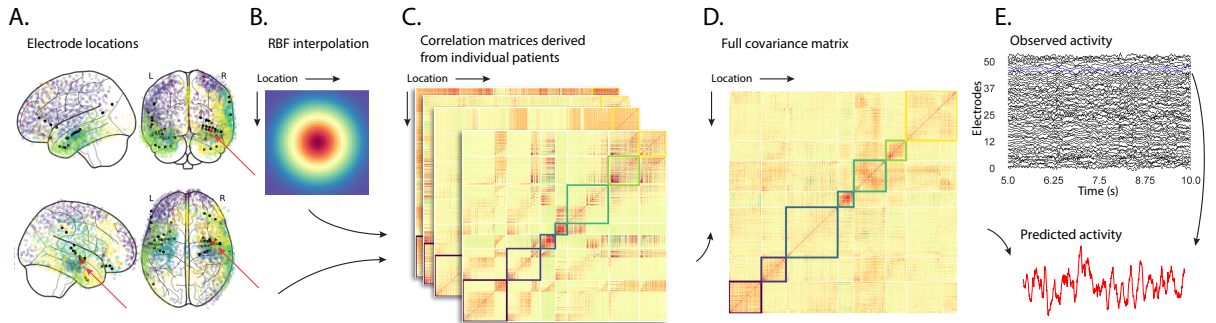


Figure 1: Methods overview. **A. Electrode locations.** Each dot reflects the location of a single electrode in dataset 1, colored according to 7 factor labels (see Panel D for details). One patient’s electrode locations are highlighted in black and the to-be-reconstructed recording location is highlighted in red. **B. Radial basis function (RBF).** Each electrode contributed by the patient (black) weights on the full set of locations under consideration (all dots in Panel A, defined as \bar{R} in the text). The weights fall off with positional distance (in MNI space) according to an RBF. **C. Per-patient correlation matrices.** After computing the pairwise correlations between the recordings from each patient’s electrodes, we use RBF-weighted averages to estimate correlations between all locations in \bar{R} . We obtain an estimated full-brain correlation matrix using each patient’s data. **D. Combined correlation matrix.** We estimate a single full-brain correlation matrix by averaging the patient-specific correlation matrices. We sort the resulting correlation matrix based on 7 factor labels obtained from k-means clustering [26]). **E. Reconstructing activity throughout the brain.** Given the observed activity from the patient’s electrodes and the estimated correlation matrix (Panel D), we can compute a maximum likelihood estimate of the voltage trace at any location in \bar{R} . An example reconstruction (at the red dot in Panel A) is shown in red, and the actual recording at that location is highlighted above in blue.

tient electrode locations weight matrix, W . Specifically, W approximates how informative the recordings at each location in R_s are in reconstructing activity at each location in \bar{R} , where the contributions fall off with an RBF according to the distances between the corresponding locations:

$$W(i, j) = \text{rbf}(i|j, \lambda). \quad (5)$$

Given this weight matrix, W , and the observed inter-electrode correlation matrix for patient s , \bar{C}_s , we can estimate the correlation matrix for all locations in \bar{R} (Fig. 1C) using:

$$\hat{N}_s(x, y) = \sum_{i=1}^{|R_s|} \sum_{j=1}^{i-1} W(x, i) \cdot W(y, j) \cdot z(\bar{C}_s(i, j)) \quad (6)$$

$$\hat{D}_s(x, y) = \sum_{i=1}^{|R_s|} \sum_{j=1}^{i-1} W(x, i) \cdot W(y, j). \quad (7)$$

Intuitively, we construct an estimated correlation matrix from each individual patient's data (Fig. 1C) using Equations 6 & 7, then we sum across these estimates for S patients and divide (see Equations 8) to obtain the expected correlation matrix, \hat{K} (Fig. 1D):

$$\hat{K} = r \left(\frac{\sum \hat{N}_s}{\sum \hat{D}_s} \right). \quad (8)$$

Now we can use the following intuition: given (i) the observed responses from a limited set of locations in R_s (Y_s) and (ii) how each location's responses relate to all other responses (\hat{K}), we can estimate the LFP data from patient s , for any arbitrary location in \bar{R} (Fig. 1E).

Let α be the set of indices of patient s 's electrode locations in \bar{R} , and let β be the set of indices of all other locations in \bar{R} . In other words, β reflects the locations in \bar{R} where we did

¹³¹ not observe a recording for patient s (these are the recording locations we will want to fill in
¹³² using Super EEG). We can sub-divide \hat{K} as follows:

$$\hat{K}_{\beta,\alpha} = \hat{K}(\beta, \alpha), \text{ and} \quad (9)$$

$$\hat{K}_{\alpha,\alpha} = \hat{K}(\alpha, \alpha). \quad (10)$$

¹³³ Here $\hat{K}_{\beta,\alpha}$ stores the correlations between the “unknown” activity at the locations in β and the
¹³⁴ observed activity at the locations in α , and $\hat{K}_{\alpha,\alpha}$ stores the correlations between the observed
¹³⁵ recordings (at the locations in α).

¹³⁶ Let $Y_{s,k,\alpha}$ be the number-of-timepoints (T) by $\text{length}(\alpha)$ matrix of (observed) voltages from
¹³⁷ the electrodes in α during session k from patient s . Then we can estimate the voltage from
¹³⁸ patient s ’s k^{th} session at the locations in β using [27]:

$$Y_{s,k,\beta} = ((\hat{K}_{\beta,\alpha} \cdot \hat{K}_{\alpha,\alpha}^{-1}) \cdot Y_{s,k,\alpha}^T)^T. \quad (11)$$

¹³⁹ This equation is the foundation of the Super EEG algorithm. Whereas we observe the recordings
¹⁴⁰ only at the locations in α , Equation 11 allows us to estimate the recordings at all locations in
¹⁴¹ β , which we can define *a priori* to include any locations we wish, throughout the brain. This
¹⁴² yields estimates of the time-varying voltages at *every* location in \bar{R} .

¹⁴³ We designed our approach to be agnostic to electrode impedances, as electrodes that do not
¹⁴⁴ exist do not have impedances. Therefore our algorithm recovers voltages in standard deviation
¹⁴⁵ (z -scored) units rather than attempting to recover absolute voltages. (This property reflects
¹⁴⁶ the fact that $\hat{K}_{\beta,\alpha}$ and $\hat{K}_{\alpha,\alpha}$ are correlation matrices rather than covariance matrices.) Also,
¹⁴⁷ note that Equation 11 requires computing a T by T matrix, which can become computationally
¹⁴⁸ intractable when T is very large (e.g. for the patient highlighted in Fig. 2, $T = 20458799$).

¹⁴⁹ However, we may approximate $Y_{s,k,\beta}$ in a piecewise manner by filling in $Y_{s,k,\beta}$ in blocks of size
¹⁵⁰ b samples (using the corresponding samples from $Y_{s,k,\alpha}$). In our computations we set $b = 25000$.

¹⁵¹ The Super EEG algorithm described above and in Figure 1 allows us to estimate (up to a
¹⁵² constant scaling factor) LFPs for each patient at all arbitrarily chosen locations in the set \bar{R} ,
¹⁵³ even if we did not record that patient’s brain at all of those locations.

¹⁵⁴ Results

¹⁵⁵ To test the accuracy with which the Super EEG algorithm reconstructs activity throughout the
¹⁵⁶ brain, we held out each electrode from the full dataset in turn and treated it as unobserved. We
¹⁵⁷ then asked: how closely did each of the Super EEG-reconstructed LFPs match the observed
¹⁵⁸ data? We sought to evaluate both the overall reconstruction accuracy as well as how reconstruc-
¹⁵⁹ tion accuracy varied as a function of implantation location.

¹⁶⁰ We first examined raw LFP traces and their associated Super EEG-derived reconstructions.
¹⁶¹ Figure 2A displays the LFP from the red electrode in Figure 1A, and its associated reconstruc-
¹⁶² tion, during a 5 s time window during one of the patient’s 6 recording sessions. Figure 2B
¹⁶³ displays a 2D histogram of the observed versus reconstructed voltages for every sample across
¹⁶⁴ 14.2 total hours of recordings from that patient (correlation: $r = 0.91, p < 10^{-10}$). Although the
¹⁶⁵ Super EEG algorithm recovered the recordings from this electrode well, we sought to quantify
¹⁶⁶ the algorithm’s performance across the full dataset.

¹⁶⁷ Holding out each electrode from each patient in turn, we computed the average correla-
¹⁶⁸ tion (across recording sessions) between the Super EEG-reconstructed voltage traces and the
¹⁶⁹ observed voltage traces from that electrode. For each reconstruction, we estimated the full-
¹⁷⁰ brain correlation matrix using every *other* patient’s data (i.e. every patient except the one who
¹⁷¹ contributed the to-be-reconstructed electrode data). In our analyses, we then substituted the
¹⁷² average correlation matrix computed after excluding patient s ’s data for \hat{K} in Equations 9 and

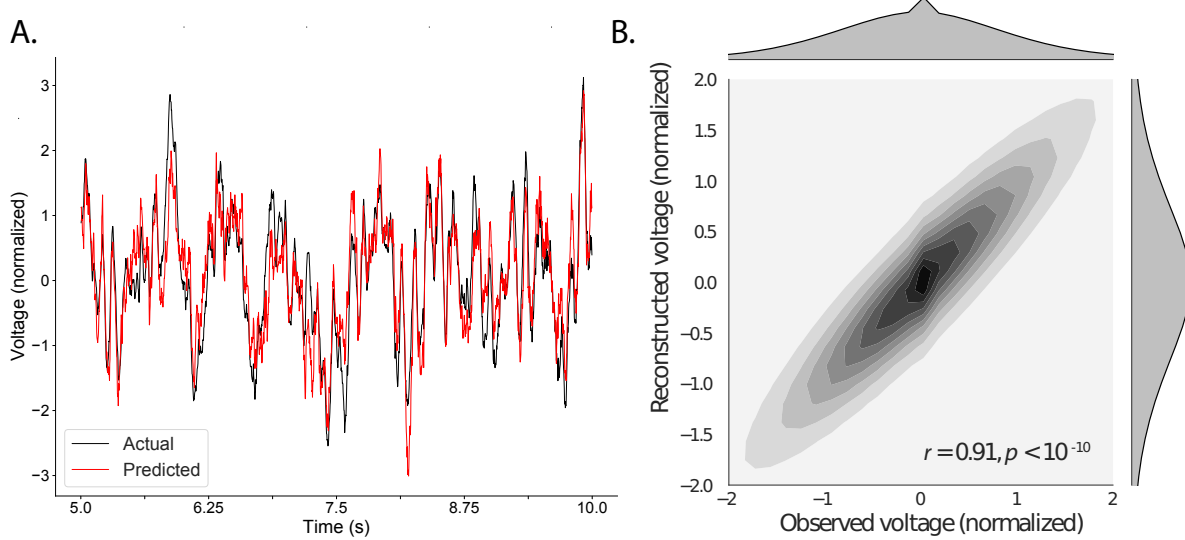


Figure 2: Observed and reconstructed LFP from a single electrode. A. Example LFP. A 2 s recording from the blue electrode in Figure 1A is displayed in red, and the reconstructed LFP during the same time window is shown in black. All voltages are plotted in standard deviation units. **B. Observed versus reconstructed voltages over 14.2 hours.** The 2D histogram reflects the relation between distributions of observed versus reconstructed voltages from one patient, across the 14.2 hours of recorded data collected in 6 recording sessions. The correlation reported in the panel is between the observed and reconstructed voltages.

173 10. This step ensured that the data we were reconstructing could not also be used to estimate
174 the between-location correlations that drove the reconstructions via Equation 11 (otherwise the
175 analysis would be circular).

176 We obtained a single correlation coefficient for each electrode location in \bar{R} , reflecting how
177 well the Super EEG algorithm was able to recover the recording at that location by incorpo-
178 rating data across patients (Across shown in black, see Fig. 3A). We also reconstructed activ-
179 ity for each electrode using a model trained on the remaining electrodes from only that pa-
180 tient, to account for reconstruction accuracy attributed to volume conductance alone (Within
181 shown in gray, see Fig. 3A). For the first dataset, we compared these two distributions of
182 correlation coefficients (paired t -test between z -transformed mean correlation coefficients by
183 patient: $t(66) = 9.64, p < 10^{-10}$). We repeated this analysis on a similar dataset (Fig. 3C)
184 with similar results (paired t -test between z -transformed mean correlation coefficients by pa-
185 tient: $t(23) = 6.93, p < 10^{-5}$). This is an especially conservative test, given that the Super
186 EEG reconstructions exclude (from the correlation matrix estimates) all data from the patient
187 whose data is being reconstructed. Furthermore, we also replicated this finding for each in-
188 dependent experiment within dataset 2 (Fig. S3 (paired t -test between z -transformed mean
189 correlation coefficients by patient for experiment 1: $t(23) = 6.23, p < 10^{-5}$ and experiment 2:
190 $t(23) = 6.62, p < 10^{-5}$). That the Super EEG-derived correlations were reliably stronger than
191 these correlations obtained using a volume conductance null model is exciting for two reasons.
192 First, it implies that distant electrodes provide additional predictive power to the data recon-
193 structions beyond the information contained in nearby electrodes. Second, it implies that the
194 spatial correlations driving the Super EEG algorithm are, to some extent, shared across people.

195 We were interested in the task specific contributions to the reconstruction accuracy. Each
196 patient in the second dataset participated in two free recall experiments. We ran similar
197 analyses for both experiments and found that activity was best reconstructed when limiting the

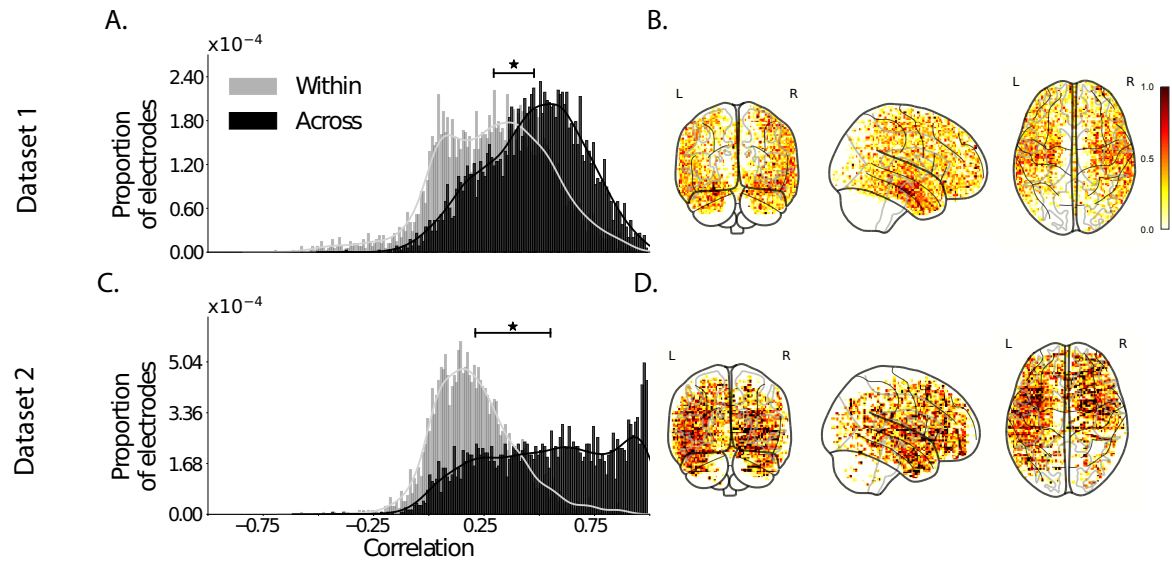


Figure 3: Reconstruction quality. A. & C. Distributions of correlation coefficients. Across all electrodes from all patients in the labeled dataset, the panel displays the distribution of correlations between the observed and reconstructed LFP data using models trained on data from all other patients (Across, in black) and all other electrodes from the same patient (Within, in gray). **B. & D. Correlation maps.** The glass brain maps display the average correlation between the observed LFP data and the across-subjects model reconstructed data by location, for each labeled experiment.

198 training data to within task, as opposed to across task or incorporating data from both tasks (Fig.
199 S1 (mean reconstruction accuracy incorporating data within task: 0.55, across task: 0.37, all
200 tasks: .50)). Although reconstruction accuracy in the across task analysis was still better than
201 the volume conductance model alone (paired *t*-test between *z*-transformed mean correlation
202 coefficients by patient: $t(47) = 5.65, p < 10^{-5}$), these results suggests that having a common
203 tasks for patients may yield better reconstruction accuracy.

204 We also wondered whether reconstruction quality (measured as the correlation between the
205 observed and reconstructed data) varied with the electrode locations (Fig. 3B & D). In general,
206 reconstruction quality remained high throughout the brain. Although reconstruction accuracy
207 appeared high in the medial temporal lobe, which is a common epileptic focus (and therefore a
208 common target for electrode implantation), we observed a weak but statistically reliable nega-
209 tive correlation between reconstruction quality and electrode density (defined as the proportion
210 of electrodes within 20 MNI units for each location; dataset 1: $r = -0.07, p < 10^{-5}$, dataset 2:
211 $r = -0.16, p < 10^{-10}$). This provides some evidence that our reconstruction accuracy results
212 cannot be driven only by volume conductance. Qualitatively, it appeared that the distribution
213 of electrodes was similar across the datasets, suggesting potential commonalities of target loca-
214 tions across patients and similarities in surgical decisions. Indeed, we found a relatively strong
215 correlation between the electrode densities within the two datasets (defined as the proportion of
216 electrodes within 20 MNI units for each 34686 voxels (Fig. 4A, B); $r = 0.57, p < 10^{-10}$).

217 In addition to exploring how reconstruction quality varies with location, we also wondered
218 whether there might be effects of electrode placements on reconstruction quality. For example,
219 are there particular implantation locations that yield especially high reconstruction accuracies at
220 other locations throughout the brain? To gain insights into this questions, we computed the aver-
221 age reconstruction correlation for each patient, then computed the average patient reconstruction
222 correlation for any patients who had electrodes within a 20 MNI unit diameter sphere centered

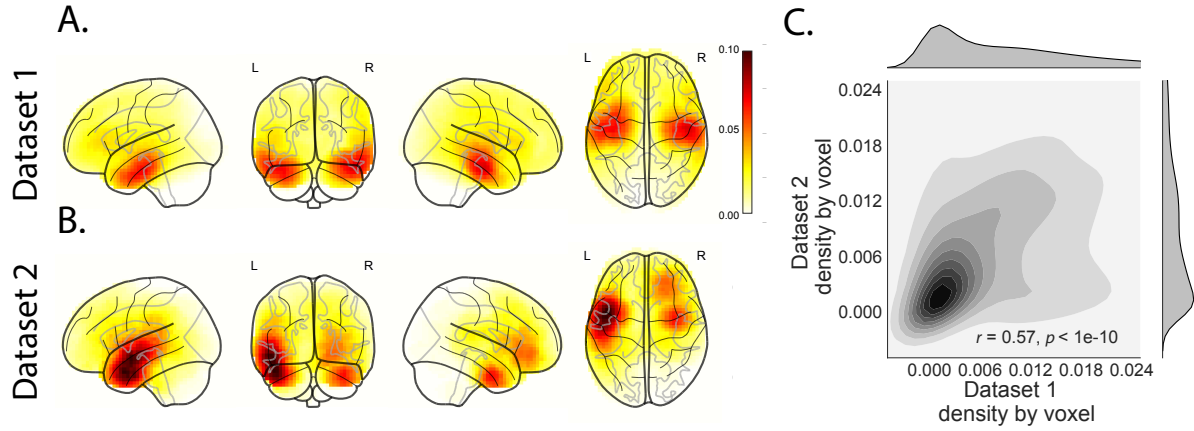


Figure 4: Sampling density and reconstruction quality. **A. & B.** The glass brain maps show sampling density by voxel location for dataset 1 and dataset 2. **C.** Correlation of sampling density by voxel location for dataset 1 vs. dataset 2.

on each voxel location. The resulting maps highlight the locations of implanted electrodes from patients whose reconstructions were especially accurate (Fig. 5A and B). We found that the most informative locations were consistent across datasets which lends support to the notion that different electrode location are more informative about activity across patients (Fig. 5C); $r = 0.22, p < 10^{-10}$). The locations in dark red might therefore be good candidate implantation targets for neurosurgeons and neurologists who wish to use Super EEG to reconstruct full-brain electrophysiological signals. The above findings, that one can infer brain activity throughout a person's brain using recordings from a limited number of locations from that person's brain in conjunction with recordings from other people's brains, have deep implications for the structure of brain data. The first implication is that the correlational structure of different people's brain data is largely preserved across individuals. Despite recent evidence that different people have stable but reliably different resting state connectome [3], our results suggest that the correlational structure of different people's brain data is preserved enough across individuals to provide meaningful information.

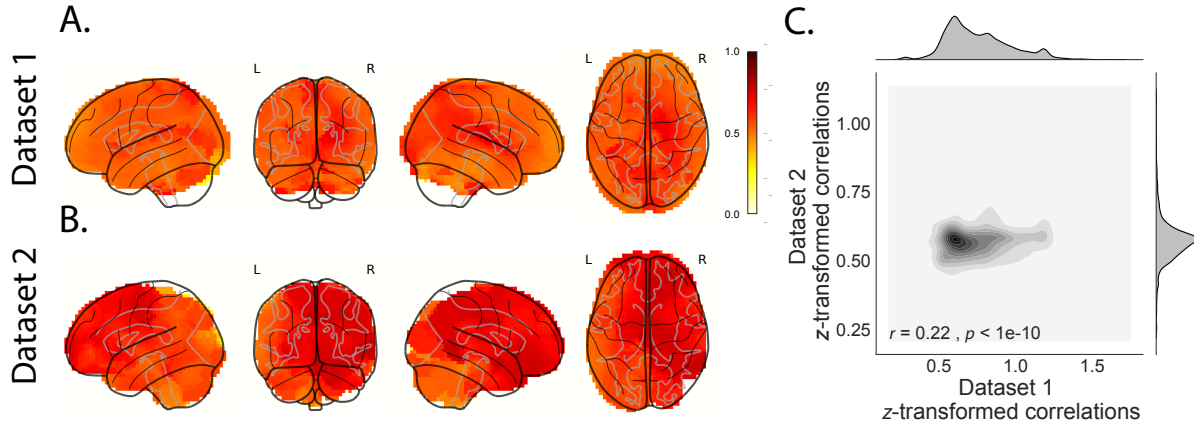


Figure 5: **Most informative electrode locations.** **A. & B.** The glass brain maps displays the average reconstruction correlations (by patient, across all electrodes) for patients with electrodes within a 20 MNI unit diameter sphere centered on each location for dataset 1 and dataset 2. **C.** Correlation between z-transformed correlations by voxel for dataset 1 vs. dataset 2.

Discussion

Super EEG infers full-brain activity patterns by leveraging correlations in those patterns of brain activity within and across people. Although the approach may, in principle, be used to infer brain activity *anywhere* in the brain, the inferences perform slightly better for regions with dense electrode sampling across patients. (Taken to the logical extreme, we could not hope to accurately recover activity patterns from brain areas where no recordings existed from any patient.) As more data are included in the inference procedure, this suggests that reconstruction accuracy should improve.

A fundamental assumption of the Super EEG algorithm is that the data covariance matrix is stable over time and across people. This is a useful simplification. However, a growing body of evidence from the fMRI community suggests that the data covariance matrix changes in meaningful ways over time (for example, the data covariance matrix changes from moment-to-moment during story listening, serving as a unique “fingerprint” for each moment of the story; further, these task-driven timepoint-specific covariance fingerprints appear to be largely

preserved across people [28, 29]). These findings indicate that the full-brain covariance matrix is not stable over time. Other recent work has shown that people's resting state connectivity matrices may be used to uniquely identify individuals and predict fluid intelligence scores [3]. This indicates that the full-brain covariance matrix is not stable across people. If the fundamental stability assumptions that Super EEG relies on are violated, how can the Super EEG algorithm still accurately recover LFP data? It is important to recognize that the fact that variability (over time or across people) is predictive (e.g. of cognitive states during story listening or fluid intelligence scores) does not necessarily mean that this variability is large in magnitude. Rather, we have long known that brain structure is tightly preserved across individuals (and over time, at least on the timescale of typical clinical and experimental recording sessions), and any functional changes must occur within the framework of the underlying structural anatomy. Nevertheless, one could imagine future improvements to the Super EEG approach that leverage resting state fMRI or structural data [e.g. diffusion tensor imaging (DTI)] to estimate Bayesian priors over the correlation matrices inferred, in the current framing, using only ECoG data. Further, relaxing the assumption that the covariance matrix is stable (over time and/or across people), and/or incorporating more detailed brain conductance models (e.g. informed by structural MRI scans) may improve the predictive performance of the approach.

One potential limitation of the Super EEG approach is that the above assumption of covariance stability across people may be violated even more if different patients are performing different cognitive tasks. To understand of the extent to which the current findings generalize across cognitive tasks, we replicated our initial findings using a dataset in which patients participated in two tasks, and limited the training data to either within task, across task, or using both tasks. Since we found the most accurate reconstructions using task-specific data, this would suggest building up new databases for estimating each task-specific covariance matrix. Or, using a more sophisticated approach, one could create a hierarchical model whereby each

276 task-specific covariance matrix was modeled as a perturbation of a “global” task-unspecific
277 covariance matrix (which could in turn be informed by fMRI or DTI data).

278 A second potential limitation of the Super EEG approach is that it does not provide a nat-
279 ural means of estimating the precise timing of single-neuron action potentials. Prior work has
280 shown that gamma band and broadband activity in the LFP may be used to estimate the firing
281 rates of neurons that underly the population contributing to the LFP [30]. Because Super EEG
282 reconstructs LFPs throughout the brain, one could in principle use gamma or broadband power
283 in the reconstructed signals to estimate the corresponding firing rates (though not the timings of
284 individual action potentials).

285 Beyond providing a means of estimating ongoing activity throughout the brain using already
286 implanted electrodes, our work also has implications for where to place the electrodes in the first
287 place. Electrodes are typically implanted to maximize coverage of suspected epileptogenic tis-
288 sue. However, our findings suggest that this approach could be further optimized. Specifically,
289 one could leverage not only the non-invasive recordings taken during an initial monitoring pe-
290 riod (as is currently done), but also recordings collected from other patients. We could then ask:
291 given everything we know about the other patients and from the scalp recordings of this new
292 patient, where should we place a fixed number of electrodes to maximize our ability to map
293 seizure foci? As shown in Figure 5, recordings from different locations are differently informa-
294 tive in terms of reconstructing the spatiotemporal patterns throughout the brain. This property
295 might be leveraged in decisions about where to surgically implant electrodes in future patients.

296 **Concluding remarks**

297 Over the past several decades, neuroscientists have begun to leverage the strikingly profound
298 mathematical structure underlying the brain’s complexity to infer how our brains carry out com-
299 putations to support our thoughts, actions, and physiological processes. Whereas traditional

300 beamforming techniques rely on geometric source-localization of signals measured at the scalp,
301 here we propose an alternative approach that leverages the rich correlational structure of a large
302 dataset of human intracranial recordings. In doing so, we are one step closer to observing, and
303 perhaps someday understanding, the full spatiotemporal structure of human neural activity.

304 **Code availability**

305 We have released an open-source SuperEEG Python toolbox. All of the code used in this
306 manuscript is on GitHub, and the code may be shared using a GitHub account accessible to
307 the reviewers upon request.

308 **Data availability**

309 The dataset analyzed in this study was generously shared by Michael J. Kahana. A portion of
310 the dataset may be downloaded [here](#).

311 **Acknowledgements**

312 We are grateful for useful discussions with Luke J. Chang and Matthijs van der Meer. We are
313 also grateful to Michael J. Kahana for generously sharing the ECoG dataset we analyzed in our
314 paper, which was collected under NIMH grant MH55687 to MJK. Our work was also supported
315 in part by NSF EPSCoR Award Number 1632738. The content is solely the responsibility of the
316 authors and does not necessarily represent the official views of our supporting organizations.

317 **Author Contributions**

318 J.R.M conceived and initiated the project. L.L.W.O. and A.C.H. performed the analyses. J.R.M.
319 and L.L.W.O. wrote the manuscript.

320 **Author Information**

321 Reprints and permissions information is available at www.nature.com/reprints. The authors de-
322 clare no competing financial interests. Readers are welcome to comment on the online version
323 of the paper. Publisher's note: Springer Nature remains neutral with regard to jurisdictional
324 claims in published maps and institutional affiliations. Correspondence and requests for mate-
325 rials should be addressed to J.R.M. (jeremy.r.manning@dartmouth.edu).

326 **References and Notes**

- 327 [1] R. J. Sawyer, *The Terminal Experiment* (HarperPrism, 1995).
- 328 [2] J. R. Manning, *et al.*, *NeuroImage* (2018).
- 329 [3] E. S. Finn, *et al.*, *Nature Neuroscience* **18**, 1664 (2015).
- 330 [4] N. B. Turk-Browne, *Science* **342**, 580 (2013).
- 331 [5] B. J. Casey, J. N. Giedd, K. M. Thomas, *Biological Psychology* **54**, 241 (2000).
- 332 [6] J. Talairach, P. Tournoux, *Co-planar stereotaxic atlas of the human brain* (Verlag,
333 Stuttgart, 1988).
- 334 [7] N. Jahanshad, *et al.*, *NeuroImage* **81**, 455 (2013).
- 335 [8] S. Mori, *et al.*, *NeuroImage* **40**, 570 (2008).
- 336 [9] C. O. Becker, *et al.*, *Scientific Reports* **8**, <https://doi.org/10.1038/s41598> (2018).
- 337 [10] O. Sporns, R. F. Betzel, *Annual Review of Psychology* **67**, 613 (2016).
- 338 [11] P. B. Sederberg, M. J. Kahana, M. W. Howard, E. J. Donner, J. R. Madsen, *Journal of*
339 *Neuroscience* **23**, 10809 (2003).

- 340 [12] P. B. Sederberg, *et al.*, *Cerebral Cortex* **17**, 1190 (2007).
- 341 [13] P. B. Sederberg, *et al.*, *Psychological Science* **18**, 927 (2007).
- 342 [14] J. R. Manning, S. M. Polyn, G. Baltuch, B. Litt, M. J. Kahana, *Proceedings of the National
343 Academy of Sciences, USA* **108**, 12893 (2011).
- 344 [15] J. R. Manning, M. R. Sperling, A. Sharan, E. A. Rosenberg, M. J. Kahana, *The Journal of
345 Neuroscience* **32**, 8871 (2012).
- 346 [16] Y. Ezzyat, *et al.*, *Current Biology* **27**, 1 (2017).
- 347 [17] P. C. Horak, *et al.*, *Epilepsia* **58**, 373 (2017).
- 348 [18] J. E. Kragel, *et al.*, *NeuroImage* **155**, 70 (2017).
- 349 [19] M. T. Kucewicz, *et al.*, *Brain* **140**, 1337 (2017).
- 350 [20] J.-J. Lin, *et al.*, *Hippocampus* **27**, 1040 (2017).
- 351 [21] E. A. Solomon, *et al.*, *Nature Communications* **In press** (2018).
- 352 [22] C. T. Weidemann, *et al.*, *Journal of Experimental Psychology: General* **In press** (2018).
- 353 [23] Y. Ezzyat, *et al.*, *Nature Communications* **9**, <https://www.doi.org/10.1038/s41467> (2018).
- 354 [24] M. T. Kucewicz, *et al.*, *Brain* **141**, 971 (2018).
- 355 [25] J. R. Manning, R. Ranganath, K. A. Norman, D. M. Blei, *PLoS One* **9**, e94914 (2014).
- 356 [26] B. T. T. Yeo, *et al.*, *Journal of Neurophysiology* **106**, 1125 (2011).
- 357 [27] C. E. Rasmussen, *Gaussian processes for machine learning* (MIT Press, 2006).
- 358 [28] E. Simony, C. J. Honey, J. Chen, U. Hasson, *Nature Communications* **7**, 1 (2016).

³⁵⁹ [29] J. R. Manning, *et al.*, *bioRxiv* p. 106690 (2017).

³⁶⁰ [30] J. R. Manning, J. Jacobs, I. Fried, M. J. Kahana, *The Journal of Neuroscience* **29**, 13613
³⁶¹ (2009).